Chapter 4

Vanadium Sesquioxide

After the previous chaptering (Chapter 3), in which we described the first strategy to achieve ultrafast switch in solid state systems, we will now turn the attention to the second method consisting in the investigation of the coherent-control of the insulator-to-metal transition in correlated materials. In particular, in Chapter 4, the main properties of the prototype Mott insulator vanadium sesquioxide (V_2O_3) will be introduced. After an initial overview of the rich phase diagram exhibited by this compound, we will focus on its structural, electronic, and optical properties and how they change across the temperature-driven phase transition. Then, the recently investigated light-induced phase transition will be presented, with particular emphasis on the results obtained in optical time-resolved experiments.

4.1 Material Properties and Equilibrium Insulator-to-Metal Transition

4.1.1 Phase Diagram

In the last fifteen years, the condensed matter community paid more and more attention to vanadium sesquioxide (V_2O_3) compound since it represents the ideal platform for the theoretical and experimental study of the Mott insulator-to-metal transition (IMT) [Imada et al., 1998]. Starting from the successful growth of the first single crystals of $(V_{1-x}Cr_x)_2O_3$ [McWhan et al., 1969], the study of the transitions involving different phases of this compound triggered

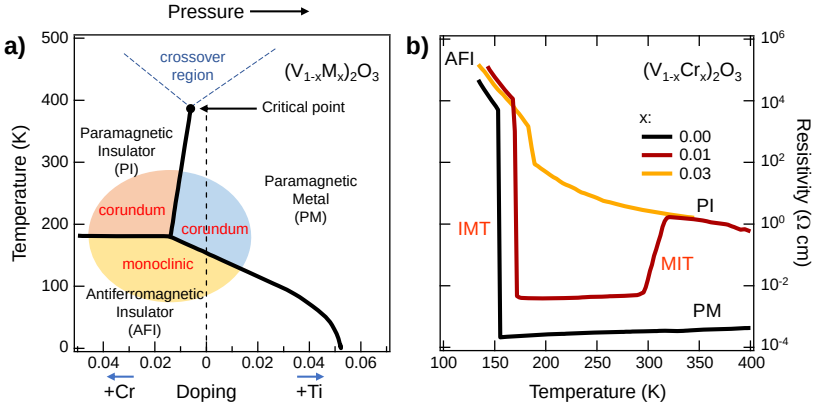

Figure 4.1: **Insulator-to-Metal Transition in $(V_{1-x}M_x)_2O_3$.** (a). Phase diagram of the insulator-to-metal transition (IMT) for doped vanadium sesquioxide systems. Image adapted from [Hansmann et al., 2013] (b). Resistivity as a function of the temperature during cooling cycle for $(V_{1-x}Cr_x)_2O_3$ single crystal samples with different doping level (x). Image adapted from [Kuwamoto et al., 1980]

the scientific research up to make V_2O_3 the prototypical Mott-Hubbard material [Imada et al., 1998]. The diagram in Fig. 4.1a summarizes the different phases that characterize the physical properties of bulk $(V_{1-x}M_x)_2O_3$ (where the doping element M is Cr, chromium, or Ti, titanium) as a function of temperature and doping (x) [McWhan et al., 1973]. The structural properties will be addressed in more detail in Sec. 4.1.2.

At ambient conditions (1 atm, RT) V_2O_3 compound shows a paramagnetic metallic (PM) phase. When the temperature decreases (black dotted line in Fig. 4.1a), V_2O_3 undergoes a transition ($T \approx 160$ K) towards the antiferromagnetic insulating (AFI) phase, together with a structural change of the lattice from corundum to monoclinic. As displayed in Fig. 4.1b (black line, $x = 0.00$), the MIT corresponds to a a sharp increase in the resistivity of several orders of magnitude [Kuwamoto et al., 1980]. Starting from this behaviour, however, the properties of V_2O_3 can be dramatically modified by doping with other chemical elements. For example, as shown in Fig. 4.1a, a Ti-doping level exceeding ~ 0.05 determines a quenching of the IMT [McWhan et al., 1973]. On the other hand, by introducing chromium, the system at RT can be driven from the paramagnetic metallic to the paramagnetic insulating (PI) phase. Interestingly, according to the value of the Cr-doping level, an initial AFI phase at low temperature can undergo one ($x > 0.018$) or two ($0 < x < 0.018$) transitions as the temperature is increased [Kuwamoto et al., 1980]. In the former case, although a small variation at the structural transition, the system maintains an overall semiconducting behaviour (without any IMT) as confirmed by the resistivity

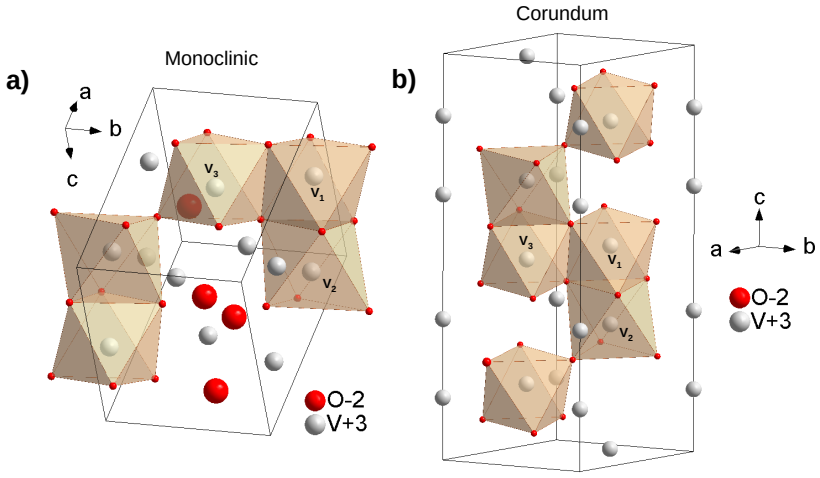

Figure 4.2: **Crystal Structure of V_2O_3.** (a) Unit cell of the low-temperature monoclinic phase. The atom positions are taken from [Tenailleau et al., 2003]. (b) Unit cell of the high-temperature corundum phase. The atom positions are taken from [Rozier et al., 2002].

curve (yellow line, $x = 0.03$) reported in Fig. 4.1b [Kuwamoto et al., 1980]. On the latter case, the system undergoes first a transition towards the PM phase and, then, to the PI one (corresponding to the two sharp variations in the brown resistivity curve, $x = 0.01$, in Fig. 4.1b) [Kuwamoto et al., 1980]. It is worthy to underline the physical importance of the 0.01 Cr-doping level; indeed, for this value, at RT the system undergoes the metal-to-insulator transition not corrupted by any symmetry-breaking, *i.e.* the pure *Mott transition* [McWhan et al., 1969].

4.1.2 Structural Properties

At high temperatures (PM phase), V_2O_3 crystallizes in the trigonal corundum structure, with symmetry described by the $R\bar{3}c$ space group[McWhan and Remeika, 1970, Dernier and Marezio, 1970], see Fig. 4.2. V atoms are arranged in hexagons (honeycomb structures) on the *ab* plane while along the *c* axis pairs form, vertically aligned [Imada et al., 1998]. Each vanadium ion is surrounded by an octahedron of oxygen ions with slight trigonal distortion [Castellani et al., 1978]. When the temperature decreases, the system undergoes the transition towards the AFI phase, characterized by a monoclinic structure with symmetry group I2/a [McWhan and Remeika, 1970]. When the temperature decreases, *i.e.* the system moves from the corundum to the

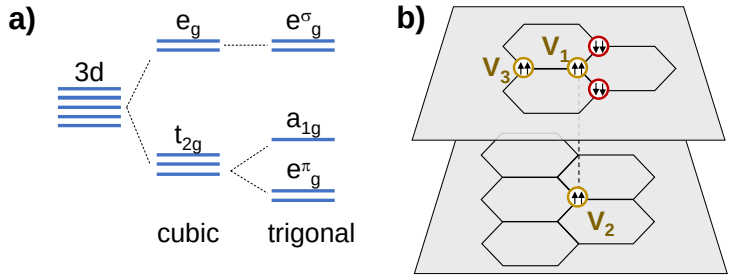

Figure 4.3: **Degeneracy Lifting and Magnetic Properties of V_2O_3.** (a) Crystal-field splitting for the 3*d* orbital angular-momentum states. The *cubic* e_g state, not affected by the trigonal distorsion, are labelled as e_g^{σ} [Hansmann et al., 2012]. The number of lines correspond to the degeneracy of the state. Adapted from [Tinkham, 1964]. (b) Ferromagnetic (gold circle) and antiferromagnetic (red circle) ordering with respect to a central atom (V_1). Adapted from [Grieger and Fabrizio, 2015]

monoclinic phase, the distances between V atoms with parallel spin increases: V_1-V_2 (distance between two hexagonal basal planes) and V_1-V_3 (hexagon edge) in Fig. 4.2 [Castellani et al., 1978]; the former determines a tilt of the V-hexagons with respect to the *ab* plane, while the latter leads to an increase of the unit cell volume of $\sim 1.4\%$ [McWhan and Remeika, 1970, Dernier and Marezio, 1970].

4.1.3 Electronic Properties

Vanadium atom has $[\mathrm{Ar}]3d^3 4s^2$ electronic configuration [Hansmann et al., 2012] and nominal valence +3 in V_2O_3 [Qazilbash et al., 2008]. Three out of five electrons are involved in covalent bonds with oxygen 2*p* states; therefore, each V atom is left with two electrons in the valence shell [Castellani et al., 1978]. The octahedral oxygen environment surrounding each V atom introduces a crystal field which splits the V-3*d* atomic orbitals into a lower t_{2g} and an upper e_g bands (three- and two-fold degenerate, respectively), as reported in Fig. 4.3a [Castellani et al., 1978].

In the corundum phase, the weak trigonal distortion (acting as a compression along one of the threefold axes of the oxygen octahedron, [Hansmann et al., 2012]), reinforced by a strong on-site Coulomb repulsion ($U \sim 2.6\,\mathrm{eV}$ [Qazilbash et al., 2008]), reduces the group symmetry of the unit cell to D_{3d} ($\equiv \bar{3}m$) and introduces a further separation of the t_{2g} band into a lower doubly degenerate e_g^{π} and single a_{1g} state [Castellani et al., 1978]. Regarding their orientation, the former lay on the *ab* plane, while the latter is aligned along the *c* axis [Hansmann et al., 2012]. The X-ray absorption

measurements performed by [Park et al., 2000] revealed that the average occupation of the e_g^π and a_{1g} orbitals in the AFI phase is of $n_{e_g^\pi} \simeq 0.83$ and $n_{a_{1g}} \simeq 0.17$ and it reduces to $n_{e_g^\pi} \simeq 0.75$ and $n_{a_{1g}} \simeq 0.25$ in the PM phase [Park et al., 2000]. Therefore, in the low-temperature condition, V_2O_3 behaves as a half-filled two-band Mott insulator [Park et al., 2000] with an effective charge gap of $2\Delta_{\text{eff}} \simeq 0.5\,\text{eV}$ [Qazilbash et al., 2008]. Moreover, the electron pairs in each V atom, coupled into spin $\mathsf{S} = 1$ configuration, give rise to an intriguing magnetic structure, as reported in Fig. 4.3b, the coupling is both ferromagnetic, with the nearest neighbour along the c axis and with one in the ab plane, and antiferromagnetic, with the remaining two nearest neighbours in the basal plane [Grieger and Fabrizio, 2015].

4.1.4 Optical Properties

A deep study of the optical properties of V_2O_3 across the IMT was conducted by Qazilbash an coworkers [Qazilbash et al., 2008]. As reported in Fig. 4.4a, the insulating behaviour of the low-temperature ($\mathsf{T} = 100\,\text{K}$) phase of V_2O_3 is highlighted by the vanishing optical conductivity (real part) at low energies, followed by an onset at the optical gap ($\simeq 0.5\,\text{eV}$). In the energy region up to 6 eV, several peaks (labelled with Roman numbers I-V) appear in the optical conductivity spectrum. According to the interpretation provided by Qazilbash and coworkers [Qazilbash et al., 2008], the high-energy peak at $\approx 4\,\text{eV}$ (V) is ascribed to interband transition from the oxygen $2p$ to the empty vanadium t_{2g} states (see the sketch in Fig. 4.4b), while the lower energy peaks (I-IV) are related to intersite vanadium-vandium transitions involving t_{2g} states [Qazilbash et al., 2008].

A significant rearrangement occurs when the temperature increases and the system reaches the paramagnetic metallic phase. In particular, the conductivity in the metallic phase ($\mathsf{T} = 200\,\text{K}$) is characterized by an overall enhancement of the spectral weight in the interband transition region below 3 eV due to two main aspects. First, the appearance of two low-lying energy peaks: the *Drude* peak v and a finite energy mode w at $\approx 0.5\,\text{eV}$. Second, a downwards shift by $0.2 - 0.3\,\text{eV}$ of the II, III, and V AFI peaks (labelled x, y, and z, respectively, in the PM phase, see Fig. 4.4c), ascribed to the decrease of the crystal-field splitting between e_g^π and a_{1g} states [Qazilbash et al., 2008].

Starting from a description of the intersite transition involving orbital multiplicity effects from Lee and coworkers [Lee et al., 2005], Qazilbash and co-workers were able to estimate some parameter related to the value of the on-site Coulomb repulsion U and Hund's rule exchange energy J_H for V_2O_3. In particular, Lee and coworkers [Lee et al., 2005] studied the optical excitations

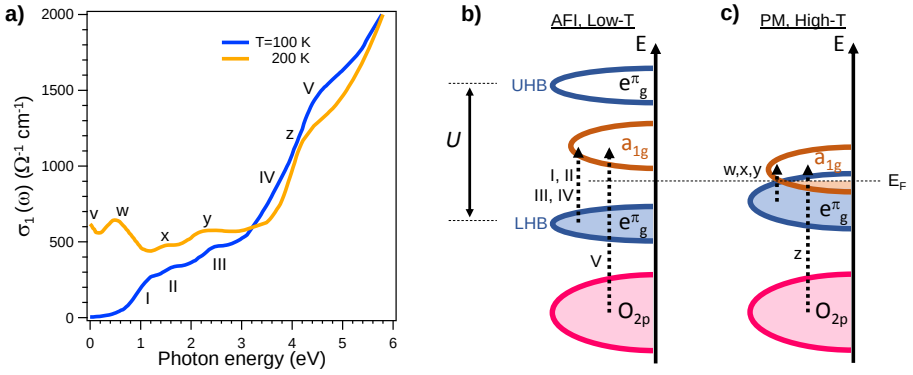

Figure 4.4: **Optical Properties and Energy Band Diagrams of V_2O_3.** (a) Optical conductivity (real part) as a function of energy for the insulating (blue line) and metallic (yellow line) phase of a thin film sample (75 nm V_2O_3 film deposited on $(10\bar{1}0)$ oriented sapphire substrate). Adapted from [Qazilbash et al., 2008]. (b, c) Sketch of the energy band diagram and of the optical transitions for the low-temperature AFI (panel b) and high-temperature PM (panel c) phase. LHB: lower Hubbard Band; UHB: upper Hubbard Band; E_F: Fermi energy level; U: on-site Coulomb repulsion. Labels in Roman numbers (lowercase letters) highlight transition peaks for the low(high)-temperature AFI (PM) phase. Adapted from [Qazilbash et al., 2008].

occurring in transition-metal oxides in the case of an orbitally degenerate Hubbard model in which transitions take place from a given state to a multiple final state. Specifically, intersite $d-d$ transition of the form

$$t_{2g}^2\, t_{2g}^2 \rightarrow t_{2g}^1\, t_{2g}^3, \tag{4.1}$$

corresponding to the situation in which each site of the system has initially two electrons (t_{2g}^2 configuration) and, after light-excitation, one electron jumps to another site (reaching t_{2g}^3 configuration) although leaving a vacancy in the original site (t_{2g}^1 configuration) [Lee et al., 2005]. The procedure adopted to build the multiple state is based on the property according to which the total wave-function of the d^n state must be antysimmetric about the exchange operation of the electrons [Lee et al., 2005, Sugano et al., 1970]. For the t_{2g}^2 and t_{2g}^3 configurations, the eigenstates are expressed through *terms* of the form ${}^{2S+1}\mathsf{D}$ with $(2\mathsf{S}+1)\cdot\dim\{\mathsf{D}\}$-fold degeneracy, where S is the total spin and D is one of the irreducible representations, whose dimension is $\dim\{\mathsf{D}\}$, of O_h-group (since the Hamiltonian describing the electron configuration is independent under transformation of this group). In particular, $\mathsf{S}=0$ or 1 ($\frac{1}{2}$ or $\frac{3}{2}$) for the t_{2g}^2 (t_{2g}^3) configuration and $\mathsf{D}=\mathsf{A}_1,\mathsf{E},\mathsf{T}_1$, or T_2 (whose dimensions are 1, 2, 3,

and 3, respectively). Following the results from Sugano, Tanabe, and Kamimura [Sugano et al., 1970]:

t_{2g}^2 **Configuration.** The Pauli principle predicts fifteen ways in which two electrons can be accomodated in the t_{2g} shell[1]. In the irreducible representation, these states corresponds to four terms: $^3\mathsf{T}_1$, $^1\mathsf{T}_2$, $^1\mathsf{E}$, and $^1\mathsf{A}_1$. The number of states in the allowed terms are: 9, 3, 2, and 1 state(s), respectively (the complete list of the wavefunctions and the corresponding energy eigenvalue for the t_{2g}^2 configuration is reported in Tab. C.1) [Sugano et al., 1970]. However, since in Eq. (4.1) the t_{2g}^2 configuration represents the initial state of the transition, therefore, the system will be in the $^3\mathsf{T}_1$ state (the ground state for this configuration) with energy $U - 3J_H$ [Lee et al., 2005].

t_{2g}^3 **Configuration.** In the irreducible representation, four terms (eigenvalues) are allowed: $^4\mathsf{A}_2$, $^2\mathsf{E}$, $^2\mathsf{T}_1$, and $^2\mathsf{T}_2$, for a total of twenty states[2] (the complete list of the wavefunctions for the t_{2g}^3 configuration is summarized in Tab. C.2) [Sugano et al., 1970]. The energy eigenvalues are reported in Tab. 4.1.

Table 4.1: **Intersite transition** $t_{2g}^2\, t_{2g}^2 \rightarrow t_{2g}^1\, t_{2g}^3$**.** Adapted from [Sugano et al., 1970, Lee et al., 2005].

Final state (t_{2g}^3)	Energy eigenvalue	Cost of the transition
$^4\mathsf{A}_2$	$3U - 9J_H$	$U - 3J_H$
$^2\mathsf{E}$	$3U - 6J_H$	U
$^2\mathsf{T}_1$	$3U - 6J_H$	U
$^2\mathsf{T}_2$	$3U - 4J_H$	$U + 2J_H$

Therefore, four transitions can occur from the initial $^3\mathsf{T}_1$ state towards one of the terms corresponding to the t_{2g}^3 configuration. For each transition, the energy cost is computed as the energy difference between the final[3] and initial state and the results are summarized in Tab. 4.1 [Lee et al., 2005]. From the calculation, three excitation energy values are obtained: $U - 3J_H$, U, and $U + 2J_H$.

[1] The number of ways in which two electrons can be accomodated in the three-fold degenerate t_{2g} shell are computed as the number of combination of six elements (considering spin degeneracy) taken two at a time: $\binom{6}{2} = 15$ [Sugano et al., 1970].

[2] According to the Pauli principle, the number of ways in which three electrons can be accomodated in the three-fold degenerate t_{2g} shell are computed as the number of combination of six elements (considering spin degeneracy) taken three at a time: $\binom{6}{3} = 20$.

[3] Since the t_{2g}^1 configuration has only one electron, the Coulomb interaction vanishes [Lee et al., 2005].

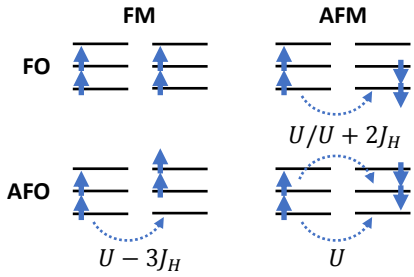

Figure 4.5: **Spin-Orbital Configurations for $d - d$ Transitions.** Diagrams of the allowed intersite $d - d$ transitions (dashed lines) in different spin-orbital situations. In the neighbouring sites, the initial spin alignment can be ferromagnetic (FM) or antiferromagnetic (AFM), while the orbital occupation can be similar (FO, ferro-orbital) or different (AFO, antiferro-orbital). Adapted from [Lee et al., 2005].

Finally, when spin and orbital correlations are taken into account, four spin/orbital scenarios are identified (see Fig. 4.5). The labels represents the spin configurations, ferromagnetic (FM) and antiferromagnetic (AFM), and orbital occupations, same (FO, ferro-orbital) or different (AFO, antiferro-orbital), for neighbouring sites. Looking at the excitation energies values, it can be stated that the lowest value occurs for the ferromagnetic spin configuration, while higher values appear for the AFM configurations [Lee et al., 2005].

As underlined by Qazilbash and coworkers, this model does not take into account the splitting of the t_{2g} band due to the trigonal distortion that gives rise to the a_{1g} and e_π^g levels [Qazilbash et al., 2008]. However, it provides useful insights on the states involved in the optical transitions and, in particular, on the magnetic coupling between the excited electrons. As mentioned, starting from this model, the values of the on-site Coulomb repulsion U and the Hund's exchange interaction energy J_H were extracted from the low-temperature optical conductivity of V_2O_3 reported in Fig. 4.4a. In particular, Qazilbash and coworkers ascribed the low-energy peak I at $\sim 1.2\,\text{eV}$ to the optical transition with final term $^4\mathsf{A}_2$ at $U - 3J_H$. Similarly, the energy peak IV at $\sim 3.6\,\text{eV}$ is assigned to the transition with final term $^2\mathsf{T}_2$ at $U + 2J_H$. Therefore, it follows that $U \simeq 2.6\,\text{eV}$ and $J_H \simeq 0.5\,\text{eV}$ [Qazilbash et al., 2008].

Before concluding this section on the optical transitions, it is useful to underline that the investigation and attribution of such transitions attracted other research groups, as Stewart and coworkers [Stewart et al., 2012], and is still under debate. The results they obtained for the energy region up to 6 eV (reported in Fig. C.2 for clarity) shows some differences with respect to those previously discussed. For our purposes, we briefly highlight the following aspect related to the optical conductivity of the low-temperature AFI phase: the optical

transition at 3.6 eV (peak IV in Fig. 4.4a) identified by Qazilbash and coworkers [Qazilbash et al., 2008], ascribed to transition within the t_{2g} orbitals, is not present in the data obtained by Stewart and coworkers [Stewart et al., 2012]. Indeed, the latter group identified only three transitions within the t_{2g} orbitals (labelled x, y, and z in Fig. C.2), whose energy positions are in agreement with peaks I (~ 1.2 eV), II (~ 1.6 eV), and III (~ 2.4 eV) in Fig. 4.4a. Therefore, by considering only the first three peaks, a small correction has to be introduced in the values of U and J_H. Similarly to the procedure adopted by Qazilbash and coworkers [Qazilbash et al., 2008], we obtain $U \simeq 1.9$ eV and $J_H \simeq 0.2$ eV.

The optical transition discussed in this section will be further considered in Chapter 5, in which we will discuss our work about the coherent manipulation of the orbital population to achieve a photo-induced phase transition (which will be described in Sec. 4.2). In particular, we will focus on the light-excitation of the orbital population involved in the optical transition corresponding to peak II (which will be labelled as *NIR Optical Transition*) and peak III (*VIS Optical Transition*) of the optical conductivity of the low-temperature insulating phase reported in Fig. 4.4a. As described in this section, according to the model by Sugano and coworkers [Sugano et al., 1970], both these transitions involve intersite $d - d$ transition between V atoms whose electrons have an antiferromagnetic alignment. Within this context, we can qualitatively characterize the final state of these two transitions on the basis of the energy *terms* as follows. Analogously to the approach followed by [Qazilbash et al., 2008], the *VIS Optical Transition* has a final t_{2g}^3 configuration corresponding to the $^2\mathsf{T}_2$ term. On the other hand, the *NIR Optical Transition* has a final t_{2g}^3 configuration corresponding to both the $^2\mathsf{E}$ and $^2\mathsf{T}_1$, since they have the same energy (see Tab. 4.1). As mentioned before, the initial t_{2g}^2 configuration for both transition corresponds to the $^3\mathsf{T}_1$ term [Sugano et al., 1970].

4.2 Photo-induced Phase Transition

In the last years, the gamut of protocols capable to achieve the insulator-to-metal transition (IMT) in vanadium sesquioxide was enriched by a new method. Indeed, in addition to temperature and doping [McWhan et al., 1969] degrees of freedom or the application of an external electric field [Guénon et al., 2013], photo-excitation revealed as a new tuning technique [Liu et al., 2011]. In 2011, Liu and coworkers [Liu et al., 2011] first demonstrated the possibility to manipulate the IMT in V_2O_3 thin film samples by a suitable light-excitation.

The transition dynamics upon photo-excitation was investigated

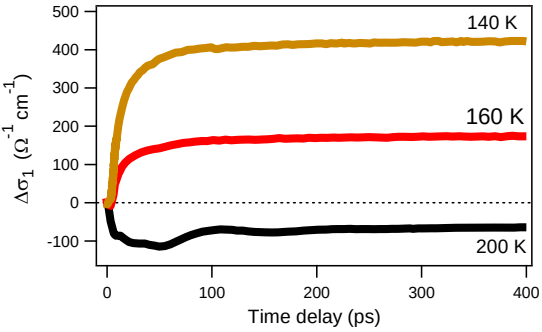

Figure 4.6: **Photo-Induced IMT in V_2O_3.** Time-resolved optical conductivity variation ($\Delta\sigma_1$) of a thin film sample (75 nm V_2O_3 deposited on oriented sapphire substrate) for different initial temperatures (lables). The measurements have been performed by a optical-pump THz-probe system. Adapted from [Liu et al., 2011].

[Liu et al., 2011] by a time-resolved experiment, in which the change of conductivity ($\Delta\sigma_1$) induced by an optical pump (1.55 eV) is detected by a THz probe ($0.1 - 2.5$ THz [Averitt and Taylor, 2002]), capable to reveal the signature of transient metallic states. Fig. 4.6 shows the results obtained when the sample is photo-excited by a fluence of 1 mJ/cm^2 at various initial temperatures: 140 K (AFI phase), 160 K (co-existing region), and 200 K (PM phase). When the system is initially in the AFI phase, the conductivity increases upon photo-excitation, suggesting the evolution towards the metallic state (gold curve in Fig. 4.6). The slow raising time (~ 20 ps), much longer than that typically occurring for electron-phonon thermalization process, is ascribed to the need for an excitation density capable to overcome the energy threshold due to nucleation and percolative growth of the metallic phase [Liu et al., 2011]. Therefore, in this photothermal transition the latent heat, associated to the first-order structural phase transition, bottlenecks the time scale for the appearance of the final metallic state properties [Liu et al., 2011]. This interpretation was supported by the behaviour of the $\Delta\sigma_1$ when the system is initially in the PM phase (black curve in Fig. 4.6). In this case, the faster raising time of ~ 3 ps (electron-phonon relaxation) suggests the absence of any percolative kinetics in the high-temperature phase [Liu et al., 2011].

Moreover, in recent years, the attention of both theoretical [Sandri and Fabrizio, 2015] and experimental [Lantz et al., 2017] works focused on the possibility to photo-induce a *non-thermal* metallic state in V_2O_3.

According to their model based on time-dependent Gutzwiller approximation, Sandri and Fabrizio [Sandri and Fabrizio, 2015] predicted that, in a Mott

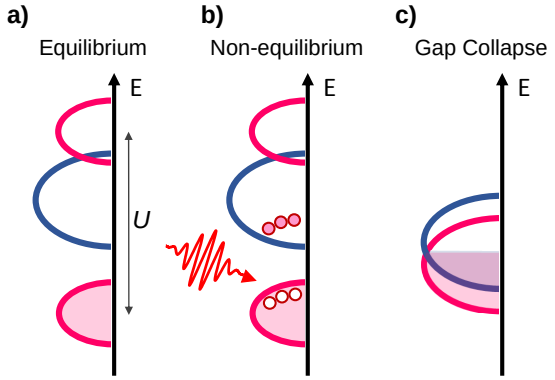

Figure 4.7: **Gap Collapse in Mott Materials.** (a) Quarter-filled two-band Mott insulator at equilibrium. (b) Orbital population imbalance. (c) Non-thermal two-band metal condition. Adapted from [Sandri and Fabrizio, 2015, Ronchi et al., 2019].

insulator, an above threshold non-equilibrium population in the upper orbital may lead to a gap collapse and lead the system towards a non-thermal metallic phase [Sandri and Fabrizio, 2015]. Specifically, they considered a quarter-filled two-band Mott insulator (see Fig. 4.7) in which the Hubbard interaction (U) opens a gap ($2\Delta_{\text{eff}}$) between an occupied and an unoccupied orbitals (at low and high energy, respectively), given by

$$2\Delta_{\text{eff}} = 2\Delta_{\text{CF}} + \frac{U}{2}\,\delta p \equiv 2\Delta_{\text{CF}} + \frac{U}{2}\,\Delta\eta, \tag{4.2}$$

where Δ_{CF} is the crystal field splitting and δp is the orbital polarization, *i.e.* the population difference between the lower and higher bands ($\delta p \simeq 1$ in the Mott insulating phase) [Sandri and Fabrizio, 2015] (the last equality comes from the definition, Eq. (2.8), of the population difference in the case of a two-level system). It is worthy to underline that the schematics in Fig. 4.7 represents the general band structure of a multi-band correlated materials near the Fermi level. In particular, it involves the orbital giving rise to the Hubbard subbands (red) and a second orbital (blue), with a different origin with respect to the former and that occupies an intermediate position. This scheme summarizes also the behaviour of V_2O_3, whose band structure is depicted in Fig. 4.4, for which the lower Hubbard band (originating from the e_g^{π} orbital) lies near the a_{1g} orbital [Qazilbash et al., 2008].

In the model described by Sandri and Fabrizio, if a population imbalance (consisting in electrons(holes) in the upper(lower) Hubbard band as in Fig. 4.7b) is induced by a suitable light excitation, according to Eq. (4.2), the reduced

orbital polarization determines a decrease of $2\Delta_{\text{eff}}$, which in turn causes a further reduction of δp. This *avalanche* process may lead to the gap collapse (Fig. 4.7c), thus temporarily pushing the system in a non-thermal metastable metal condition with overlapping bands [Sandri and Fabrizio, 2015]. Their estimations predict the gap closes when $\sim 10\%$ of electrons are promoted to the upper band, which corresponds to a fluence ~ 10 mJ/cm^2 [Sandri and Fabrizio, 2015].

These values are consistent with those reported in the experimental work by [Lantz et al., 2017], in which the appearance of a photo-induced non-thermal metallic phase (with few picoseconds lifetime) was demonstrated by a multitechnique approach [Lantz et al., 2017]. In particular, the overall non-equilibrium dynamics of the system was decomposed into the electronic and lattice contributions, the former being addressed by time-resolved photoelectron spectroscopy (trPES) while the latter being investigated by time-resolved X-ray diffraction (trXRD) and time-resolved reflectivity (trR) [Lantz et al., 2017]. This work revealed that the transition toward the non-thermal phase has an electronic nature and it is triggered by the promotion of a valuable fraction of electrons, 8% (estimated from trR with an excitation density of 8 mJ/cm^2), to the a_{1g} orbital [Lantz et al., 2017].

4.3 Nucleation and Evolution of the Metallic Phase in Vanadium Sesquioxide thin films

Recently, the combination of spatially- and time resolved techniques revealed important details about the presence of striped polydomains in the AFI phase of V_2O_3 thin films and on the formation and evolution of metallic seeds across the IMT [Ronchi et al., 2019]. Indeed, by performing spatially-resolved X-ray linear dichroism photoemission electron microscopy (XLD-PEEM) experiments at the vanadium $L_{2,3}$-edge ($\sim 513-530$ eV), Ronchi and coworkers [Ronchi et al., 2019] demonstrated that the V_2O_3 insulating phase ($\mathsf{T} = 120$ K) consists in striped nanodomains oriented along the hexagonal crystallographic axes of the material, as shown in Fig. 4.8a left-most panel [Ronchi et al., 2019]. These domains originate from a lattice distortion along one of the three equivalent edges of the hexagonal corundum unit cell and they are detected thanks to the XLD signal arising from the polarization-dependent coupling between the X-ray and the a_{1g} occupation [Ronchi et al., 2019]. When the temperature increases, metallic nanodroplets start to nucleate at the boundaries of the insulating stripes (regions within white contours in Fig. 4.8a), thus leading to a decrease in the XLD contrast compared to the one in the insulating phase. The metallic fraction (F_M) increases with increasing temperature up to the formation of an homogeneous phase ($\mathsf{T} = 180$ K) [Ronchi et al., 2019], as reported in Fig. 4.8b.

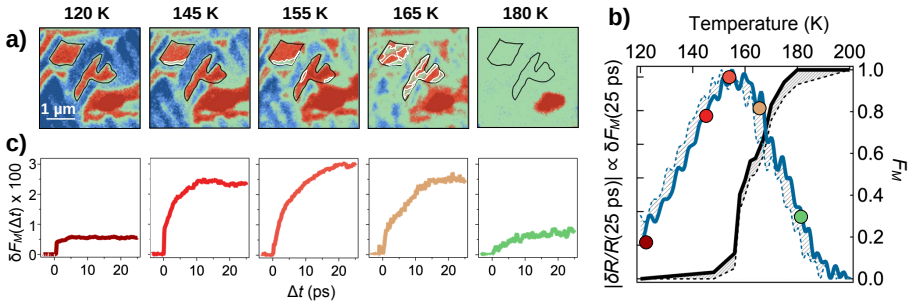

Figure 4.8: **Dynamics of Metallic Phase.** (a) XLD-PEEM images, for a V_2O_3 thin film sample (40 nm), taken in the insulating phase ($\mathsf{T} = 120\,\mathrm{K}$), at ($\mathsf{T} = 145 - 165\,\mathrm{K}$) and above ($\mathsf{T} = 180\,\mathrm{K}$) the co-existing region. (b) Temperature dependence of the metallic filling fraction F_M (black curve, right vertical axis) extracted from the images in panel (a). The blue solid line shows the temperature-dependent δF_M signal at long delays ($\Delta t = 25\,\mathrm{ps}$). (c) Time-resolved δF_M signal at 2.1 eV probe energy in the first tens of picoseconds after the pump excitation (1.55 eV, 0.3 mJ/cm^2) for the corresponding temperature values reported in panel (a). Adapted from [Ronchi et al., 2019].

To better understand the temporal dynamics of the metallic seeds, time-resolved optical spectroscopy was employed. In particular, they demonstrated that an optical broad-band probe beam in the UV-VIS spectral region (1.4-2.2 eV) is capable to reveal the photo-induced change of the metallic filling fraction (δF_M). Therefore, it was employed to detect the growth dynamics of the metallic phase induced by a NIR pump pulse (1.55 eV) whose excitation level is kept below the threshold for mesoscopic metallicity [Ronchi et al., 2019]. Fig. 4.8c summarizes, for different starting temperatures, the dynamics of δF_M as a function of the relative delay Δt between the pump and probe pulses, related to the relative reflectivity variation through

$$\frac{\delta R}{R}\left(\mathsf{T}, \omega, \Delta t\right) \simeq \tilde{\Phi}\left(F_M\left(\mathsf{T}\right), \omega\right) \cdot \delta F_M\left(\Delta t\right), \tag{4.3}$$

with $\tilde{\Phi}\left(F_M\left(\mathsf{T}\right), \omega\right)$ being a function of both the metallic filling fraction and probe frequency ω [Ronchi et al., 2019]. Compared to the time-resolved dynamics in the AFI phase (leftmost panel in Fig. 4.8c), for $\mathsf{T} > 120\,\mathrm{K}$, the presence of metallic domains with finite size leads to a longer build-up time required to the δF_M to reach the maximum value. Interestingly, as underlined by the blue curve in Fig. 4.8b, the long-delay signal ($\Delta t = 25\,\mathrm{ps}$) occurs in the temperature region between $150 - 160\,\mathrm{K}$, which corresponds to the co-existing insulating and metallic phases [Ronchi et al., 2019]. Therefore, Ronchi and coworkers [Ronchi et al., 2019] demonstrated that the growth of metallic

nanodomains embedded in the insulating phase can be triggered by a photo-induced variation of the $3d$ orbital polarization even at low excitation levels.